Journal of Computational Physics **180,** 270–296 (2002)
doi:10.1006/jcph.2002.7093

Nonreflecting Boundary Conditions for the Time-Dependent Wave Equation

Bradley Alpert,*[,1] Leslie Greengard,†[,2] and Thomas Hagstrom‡[,3]

*National Institute of Standards and Technology, 325 Broadway, Boulder, Colorado 80305; †Courant Institute of Mathematical Sciences, New York University, 251 Mercer Street, New York, New York 10012-1110; and ‡Department of Mathematics and Statistics, University of New Mexico, Albuquerque, New Mexico 87131
E-mail: alpert@boulder.nist.gov, greengard@cims.nyu.edu, and hagstrom@math.unm.edu

Received August 1, 2001; revised April 23, 2002

We describe a new, efficient approach to the imposition of exact nonreflecting boundary conditions for the scalar wave equation. We compare the performance of our approach with that of existing methods by coupling the boundary conditions to finite-difference schemes. Numerical experiments demonstrate a significant gain in accuracy at no additional cost. © 2002 Elsevier Science (USA)

1. INTRODUCTION

The scalar wave equation and Maxwell's equations govern problems in such diverse application areas as ultrasonics, seismics, underwater acoustics, antenna design, and microelectronics [1, 6, 9, 13, 17, 28, 30, 36]. In many cases, the governing equations are posed as exterior problems, and the infinite physical domain must be reduced to a finite computational domain through the use of a *nonreflecting boundary condition*.

At present, much (perhaps most) analysis is carried out in the frequency domain, since the Sommerfeld radiation condition is well understood and easy to incorporate into fast, integral equation methods used for large-scale simulation [11, 31, 32, 34, 39]. While frequency-domain methods will certainly maintain an important role in the modeling of acoustic and

[1] The work of this author was supported in part by the DARPA Applied and Computational Mathematics Program under appropriation 9770400.

[2] The work of this author was supported in part by the U.S. Department of Energy under contract DEFGO288ER25053 and by DARPA/AFOSR under contract F94620-95-C-0075.

[3] The work of this author was supported in part by NSF Grants DMS-9600146 and DMS-9971772, DARPA/AFOSR Contract F94620-95-C-0075, and, while in residence at the Courant Institute, DOE Contract DEFGO288ER25053.

0021-9991/02 $35.00

electromagnetic scattering, time-domain methods are likely to increase in popularity. They have the ability to model wide-band signals, material inhomogeneities, and nonlinearities. As a result, they have distinct advantages for the design of wide-band antennas, for the design of optical coupling and switching devices, for calculations of radar cross section for aircraft with complex coatings, for defect diagnosis of manufactured materials using ultrasonic scattering, and for medical and geophysical imaging. One of the central obstacles to the development of robust time-domain methods, however, has been the lack of accurate and efficient nonreflecting boundary conditions. Waves should impinge on the (artificial) outer boundary and disappear without reflection, but they do not. For long time integration, the reflected energy can exceed that from the true field. This is true of both local differential boundary conditions [5, 10] and (finite) "absorbing regions" [7, 27].

While there is an extensive literature on the subject (see the review articles [14, 23]), only a few methods have been proposed which are exact. Ting and Miksis suggested an interesting approach [41] that relies on Kirchhoff's formula, but which is computationally expensive. More recently, Sofronov [37] and, independently, Grote and Keller [18] have developed and implemented an integrodifferential approach in three dimensions using a spherical boundary and have demonstrated that high accuracy can be achieved at reasonable cost. In their schemes, the work is of the same order as that of the finite-difference or finite-element calculation used in the interior of the domain. In other words, for M time steps and N points on the spherical boundary, $O(MN^{3/2})$ work is required. A somewhat more general, but closely related, integral formulation is introduced in [21, 22, 38]. The fundamental analytical tool in the latter papers is what we refer to as the nonreflecting boundary kernel. In [3], we showed that the nonreflecting boundary kernel can be *compressed* and that the amount of work needed to apply the exact condition can be reduced to $O(MN \log^2 N)$ in three dimensions and $O(MN \log N)$ in two. We describe the relevant analysis in the following section. Very recently, a general approach to the compression of boundary kernels has been proposed and tested [29], which leads to similar complexity estimates. Lastly, in [35] a new exact method in three dimensions is proposed which relies on the strong Huygen's principle. As it requires the solution of an auxiliary problem on a larger domain, we expect its cost will be comparable to that of the interior solve.

Over the last few years, an important independent development has taken place in the application of integral equations to solving the wave equation. For nonreflecting boundary conditions, naive use of the relevant potential theory requires $O(MN^2)$ work. Fast "plane–wave time domain" algorithms [12, 25] are under intensive development and have reduced the cost to $O(MN \log^2 N)$ work. This approach has the significant advantage that it can be used for arbitrary geometries and achieves the same computational complexity. The associated constant, however, is rather large.

In this paper, we couple fast nonreflecting boundary conditions, developed in [3] for spherical and cylindrical boundaries and here for planar boundaries, to finite-difference solvers for the wave equation. In Section 2, we describe the exact (nonlocal) formulation, and in Section 3 we develop the fast algorithm for handling the convolution operators that arise. In Section 4, we present simple temporal and spatial discretization schemes, and in Section 5, we present a number of numerical experiments. We compare the performance of our exact scheme, local Engquist–Majda conditions [10], and the recently popular PML method [7], which uses an absorbing region to dampen undesired reflections. Our conclusions and directions for future work are discussed in Section 6.

2. EXACT NONREFLECTING BOUNDARY CONDITIONS

Let us consider the wave equation

$$u_{tt} = c^2 \Delta u \tag{1}$$

in the exterior domain $\mathbf{R}^3 \backslash \Omega$, where Ω is a finite region supported in the slab $-a < x < a$. We assume that the solution $u(x, y, z, t)$ satisfies zero initial conditions

$$\begin{matrix} u(x, y, z, t) = 0 \\ u_t(x, y, z, t) = 0 \end{matrix} \quad t \leq 0,$$

and inhomogeneous Dirichlet conditions on the boundary of Ω:

$$u(x, y, z, t) = u_{incoming}(x, y, z, t), \quad (x, y, z) \in \partial\Omega, t > 0.$$

This is typical of many acoustic-scattering problems. For the sake of simplicity, we first seek to impose nonreflecting boundary conditions along the planes $x = \pm a$. We represent the solution by Fourier transformation with respect to y and z:

$$u(x, y, z, t) = \frac{1}{2\pi} \int_{-\infty}^{\infty} \int_{-\infty}^{\infty} \hat{u}(x, \eta, \zeta, t) e^{i(y\eta + z\zeta)} \, d\eta \, d\zeta. \tag{2}$$

Suppose now that we take the Laplace transform of $\hat{u}$,

$$\tilde{u}(x, \eta, \zeta, s) = \int_0^{\infty} \hat{u}(x, \eta, \zeta, t) e^{-st} \, dt, \tag{3}$$

and consider the wave equation in terms of the function $\tilde{u}$. A straightforward calculation yields

$$[(s/c)^2 + \eta^2 + \zeta^2]\tilde{u} = \tilde{u}_{xx}.$$

This transformed equation has a right-going wave solution satisfying

$$\tilde{u}_x + \sqrt{(s/c)^2 + \eta^2 + \zeta^2}\tilde{u} = 0,$$

and a left-going wave solution satisfying

$$-\tilde{u}_x + \sqrt{(s/c)^2 + \eta^2 + \zeta^2}\tilde{u} = 0.$$

These equations form the basis for boundary conditions on the left and right boundaries. We first rewrite these last two equations in the form

$$\pm\tilde{u}_x + \frac{s}{c}\tilde{u} + [\sqrt{(s/c)^2 + \eta^2 + \zeta^2} - s/c]\tilde{u} = 0 \tag{4}$$

and note that the inverse Laplace transform of

$$\sqrt{(s/c)^2 + \eta^2 + \zeta^2} - s/c$$

is

$$\tau_w(t) = \frac{wJ_1(wct)}{t}, \tag{5}$$

where $w = \sqrt{\eta^2 + \zeta^2}$. Applying the inverse Laplace transform to (4), we obtain the (exact) boundary conditions

$$\pm\hat{u}_x(x, \eta, \zeta, t) + \frac{\hat{u}_t(x, \eta, \zeta, t)}{c} + [\tau_w * \hat{u}](x, \eta, \zeta, t) = 0, \tag{6}$$

where $*$ denotes Laplace convolution with respect to the time variable

$$(f * g)(t) = \int_0^t f(\tau)g(t - \tau)\, d\tau.$$

As above, the positive sign applies to the right boundary, and the negative to the left. We refer to $\tau_w(t)$ as the *plane nonreflecting boundary kernel*.

Remark 2.1. The nonreflecting boundary conditions in two space dimensions along lines $x = \pm a$ are essentially the same. We just set $\zeta = 0$ so that $w = \eta$ in Eq. (6).

Remark 2.2. The exact conditions (6) are nonlocal in space–time. The nonlocality in time is clear from the convolution term. The nonlocality in space is obscured by the fact that we derive (6) in the Fourier-transform domain. In physical space, we could write

$$\pm u_x(t) + \frac{u_t(t)}{c} + \mathcal{F}^{-1}[\tau_w * \mathcal{F}u](t) = 0, \tag{7}$$

where $\mathcal{F}$ denotes the Fourier transform.

2.1. Cylindrical Coordinates

The wave equation, expressed in standard cylindrical coordinates (ρ, θ, z), is given by

$$u_{tt} = c^2\left[u_{\rho\rho} + \frac{u_\rho}{\rho} + \frac{u_{\theta\theta}}{\rho^2} + u_{zz}\right]$$

with solution u that we may represent in the Fourier domain as

$$u(\rho, \theta, z, t) = \frac{1}{2\pi}\int_{-\infty}^{\infty}\sum_{n=-\infty}^{\infty}\hat{u}(\rho, n, \zeta, t)e^{in\theta + z\zeta}\, d\zeta.$$

Letting $\tilde{u}$ denote the Laplace transform of $\hat{u}(\rho, n, \zeta, t)$ with respect to t, we obtain from the wave equation the modified Bessel equation

$$\tilde{u}_{\rho\rho} + \frac{\tilde{u}_\rho}{\rho} - [(s^2/c^2 + \zeta^2) + n^2/\rho^2]\tilde{u} = 0,$$

with outgoing wave solution

$$\tilde{u}(\rho, n, \zeta, s) = K_n(\rho\sqrt{(s/c)^2 + \zeta^2}), \tag{8}$$

where K_n denotes the modified Bessel function of order n. Differentiating (8) with respect to ρ, we find that

$$\tilde{u}_\rho(\rho, n, \zeta, s) = \sqrt{(s/c)^2 + \zeta^2}\, K_n'(\rho\sqrt{(s/c)^2 + \zeta^2}),$$

which we write in the more suggestive form

$$\tilde{u}_\rho(\rho, n, \zeta, s) = \sqrt{(s/c)^2 + \zeta^2}\left[\frac{K_n'(\rho\sqrt{(s/c)^2 + \zeta^2})}{K_n(\rho\sqrt{(s/c)^2 + \zeta^2})}\right]\tilde{u}(\rho, n, \zeta, s). \tag{9}$$

Formally speaking, we could apply the inverse Laplace transform to (9). However, this leads to difficulties, since the transform of the kernel

$$\sqrt{(s/c)^2 + \zeta^2}\left[\frac{K_n'(\rho\sqrt{(s/c)^2 + \zeta^2})}{K_n(\rho\sqrt{(s/c)^2 + \zeta^2})}\right]$$

grows with s. To overcome this, we subtract the first two terms of the kernel's asymptotic expansion and write

$$\begin{aligned}\tilde{u}_\rho(\rho, n, \zeta, s) = &\left(\frac{s}{c} + \frac{1}{2\rho} + \sqrt{(s/c)^2 + \zeta^2}\,\frac{K_n'(\rho\sqrt{(s/c)^2 + \zeta^2})}{K_n(\rho\sqrt{(s/c)^2 + \zeta^2})}\right)\tilde{u}(\rho, n, \zeta, s)\\ &-\left(\frac{s}{c} + \frac{1}{2\rho}\right)\tilde{u}(\rho, n, \zeta, s).\end{aligned}$$

Taking the inverse Laplace transform now, the outgoing wave boundary condition at $\rho = b$ is

$$\hat{u}_\rho + \frac{\hat{u}_t}{c} + \frac{\hat{u}}{2b} = \sigma_{n,\zeta}(t) * \hat{u}, \tag{10}$$

where

$$\sigma_{n,\zeta}(t) = \mathcal{L}^{-1}\left(\frac{s}{c} + \frac{1}{2b} + \sqrt{(s/c)^2 + \zeta^2}\,\frac{K_n'(b\sqrt{(s/c)^2 + \zeta^2})}{K_n(b\sqrt{(s/c)^2 + \zeta^2})}\right) \tag{11}$$

is the *cylinder nonreflecting boundary kernel*.

Remark 2.3. The nonreflecting boundary conditions in two space dimensions on a circular boundary $r = b$ are essentially the same. We just set $\zeta = 0$ in Eq. (10).

2.2. Spherical Coordinates

Finally, let us consider spherical coordinates (r, θ, ϕ). Using the spherical harmonic transformation

$$u(r, \theta, \phi, t) = \sum_{n=0}^{\infty}\sum_{m=-n}^{n}\hat{u}(n, m, r, t)Y_{nm}(\theta, \phi),$$

the wave equation (after Laplace transformation) is converted to the modified Bessel equation

$$\tilde{u}_{rr} + \frac{2\tilde{u}_r}{r} - [s^2/c^2 + n(n+1)/r^2]\tilde{u} = 0.$$

Considerations similar to those outlined above yield boundary conditions at $r = b$ of the form

$$\hat{u}_r + \frac{\hat{u}_t}{c} + \frac{\hat{u}}{b} = \omega_n(t) * \hat{u}, \tag{12}$$

where

$$\omega_n(t) = \mathcal{L}^{-1}\left(\frac{s}{c} + \frac{1}{2b} + \frac{s}{c}\frac{K'_{n+1/2}(b\,s/c)}{K_{n+1/2}(b\,s/c)}\right). \tag{13}$$

We refer to $\omega_n(t)$ as the *sphere nonreflecting boundary kernel*.

3. COMPRESSION OF CONVOLUTION KERNELS

In the preceding section, we derived exact boundary conditions for planar, cylindrical, and spherical boundaries. For the planar case (6), the nonreflecting boundary kernel $\tau_w(t)$ is given in the time domain by (5). For cylindrical and spherical boundaries, however, only the Laplace transforms of the kernels $\sigma_{n,\zeta}(t)$ and $\omega_n(t)$ are given. Two tasks remain.

1. We need to invert the Laplace transform, for $\sigma_{n,\zeta}$ in (11) and ω_n in (13).
2. We need a convenient representation of the nonreflecting kernels in the time domain.

Because of the latter need, our approach will, in fact, be similar in all three settings, despite the fact that the plane kernel is known analytically. First we recall two elementary facts.

LEMMA 3.1. *Suppose that $\tilde{K}(s)$ is given as a sum of poles in the left half plane*:

$$\tilde{K}(s) = \sum_{m=1}^{M} \frac{p_m}{s + s_m},$$

with $\mathrm{Re}(s_m) > 0$. *Then its inverse Laplace transform is given by*

$$K(t) = \sum_{m=1}^{M} p_m e^{-s_m t}.$$

LEMMA 3.2. *Let*

$$f(t) = \int_0^t K(t-\tau)g(\tau)\,d\tau$$

and suppose that

$$K(t) = \sum_{m=1}^{M} p_m e^{-s_m t}.$$

Then

$$f(t) = \sum_{m=1}^{M} p_m f_m(t),$$

where

$$f_m(t) = \int_0^t e^{-s_m(t-\tau)} g(\tau)\, d\tau.$$

Moreover, $f_m(t)$ satisfies the recurrence relation

$$f_m(t+\Delta t) = e^{-s_m \Delta t} f_m(t) + \int_t^{t+\Delta t} e^{-s_m(t+\Delta t-\tau)} g(\tau)\, d\tau.$$

Remark 3.1. Lemma 3.2 eliminates the burden of history dependence. It costs only $O(M)$ work per time step to evaluate $f(t)$ recursively. Thus, even in the case of plane boundaries, it is advantageous to find efficient, accurate approximations of the nonreflecting boundary kernels in terms of a small number of poles. In the cases for the cylinder and sphere, it is essential.

LEMMA 3.3. *Let $f = K * g$, suppose that κ approximates K, and define $\phi = \kappa * g$. Then by Parseval's equality,*

$$\begin{aligned} \|\phi - f\|_2 &= \|\kappa * g - K * g\|_2 = \|\tilde{\kappa}\tilde{g} - \tilde{K}\tilde{g}\|_2 \\ &\le \left\| \frac{\tilde{\kappa} - \tilde{K}}{\tilde{K}} \right\|_\infty \|\tilde{K}\tilde{g}\|_2 = \left\| \frac{\tilde{\kappa} - \tilde{K}}{\tilde{K}} \right\|_\infty \|K * g\|_2, \end{aligned} \tag{14}$$

where the norms are taken on the real axis in the time domain and on the imaginary axis in the Laplace domain, and we assume that the Laplace transforms are all regular for $\mathrm{Re}(s) > 0$.

Alternatively, suppose we can bound the error with which $\tilde{\kappa}$ approximates $\tilde{K}$ only on the line $\mathrm{Re}(s) = \eta > 0$ *(rather than* $\mathrm{Re}(s) = 0$*). Then*

$$\|\phi - f\|_{L_2(0,T)} \le e^{\eta T} \left\| \frac{\tilde{\kappa} - \tilde{K}}{\tilde{K}} \right\|_{L_\infty(\eta + i\mathbb{R})} \|K * g\|_{L_2(0,T)}. \tag{15}$$

Remark 3.2. Lemma 3.3 shifts the task of approximating K in the time domain to approximating its transform $\tilde{K}$ in the Laplace domain. When $\tilde{K}$ cannot be conveniently approximated on the imaginary axis, only very near it, bound (15) will prove effective. We will exploit (14) for the sphere kernels ω_n, $n \in \mathbb{Z}$, and the cylinder kernels $\sigma_{n,0}$, $n > 0$, and (15) for $\sigma_{0,0}$ and the plane kernel τ_w.

3.1. The Plane Kernel

In the Laplace domain, the plane kernel takes the form

$$\sqrt{(s/c)^2 + w^2} - s/c = w(\sqrt{(s/wc)^2 + 1} - s/wc). \tag{16}$$

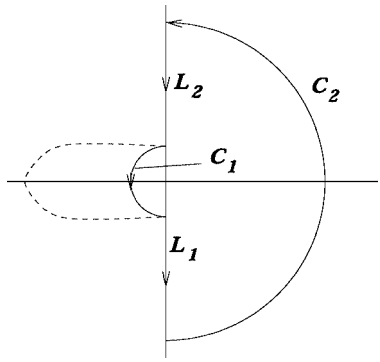

FIG. 1. The contour on which we apply Cauchy's integral formula to represent the function $(z^2+1)^{1/2}$. The branch cut is depicted by the dashed line, and C_1 is a semicircle running from i to $-i$.

By the residue theorem, for $|z| < R$, $\mathrm{Re}(z) > 0$,

$$(z^2+1)^{1/2} = \frac{1}{2\pi i}\int_{C_1+L_1+C_2+L_2} \frac{(w^2+1)^{1/2}}{w-z}\,dw,$$

where C_1 denotes the semicircle from i to $-i$ in the left half-plane, L_1 denotes the ray from $-i$ to $-iR$, C_2 denotes the semicircle from $-iR$ to iR in the right half-plane, and L_2 denotes the ray from iR to i. We assume the branch cut is taken on some contour which lies to the left of C_1 (Fig. 1). A straightforward calculation shows that, in the limit $R \to \infty$,

$$(z^2+1)^{1/2} = z + \frac{1}{\pi i}\int_{C_1} \frac{(\zeta^2+1)^{1/2}}{\zeta - z}\,d\zeta. \tag{17}$$

Combining (16) and (17), we have

$$\sqrt{(s/c)^2+w^2} - s/c = \frac{w}{\pi i}\int_{C_1} \frac{(\zeta^2+1)^{1/2}}{\zeta - s/wc}\,d\zeta. \tag{18}$$

With (18), we are close to a satisfactory representation for the plane kernel. We need simply to replace the continuum of poles on the contour C_1 with a finite number.

LEMMA 3.4. *Let $\Gamma(\tau)$, $\tau_1 \le \tau \le \tau_2$, denote a curve segment in the complex plane which lies entirely in a disk D of radius r centered at A, let $\rho(\tau)$ denote a charge density supported on Γ, and let $\phi(z)$ denote the Cauchy integral*

$$\phi(z) = \int_\Gamma \frac{\rho(\tau)}{\zeta(\tau) - z}\,d\zeta(\tau).$$

If z is a point such that $|z - A| > 2r$, then only $O(\log_2(1/\epsilon))$ poles are needed to approximate $\phi(z)$ with an error $\epsilon > 0$.

Proof. Consider first the multipole expansion of ϕ about A,

$$\phi(z) = \sum_{k=1}^{\infty} \frac{a_k}{(z-A)^k},$$

where

$$a_k = \int_\Gamma \rho(\tau)\zeta^k(\tau)\, d\zeta(\tau).$$

A simple geometric-series bound shows that

$$\left| \phi(z) - \sum_{k=1}^{p} \frac{a_k}{(z-A)^k} \right| = O(2^{-p}).$$

Thus, setting $p = \log_2(1/\epsilon)$ guarantees the desired precision. We now need to replace the truncated p-term multipole expansion for ϕ with p equispaced point sources on the boundary of D.

$$\phi(z) \approx \sum_{k=1}^{p} \frac{b_k}{z - A_k},$$

where $A_k = A + re^{2\pi ik/p}$. By matching the first p moments of this distribution to the multipole coefficients, the same precision is obtained in the far field. For this, one simply requires that

$$\sum_{k=1}^{p} b_k \zeta_k^{j-1} = a_j, \quad j = 1, \ldots, p.$$

■

Let us return now to the contour C_1 and the representation (18). We choose a line $\mathrm{Re}(z) = \eta = 1/T$ on which to compute the inverse Laplace transform, restricting its validity in the time domain to $t < T$. Consider a covering of C_1 with disks that are separated from the line $\mathrm{Re}(z) = 1/T$ by their radius, as in Fig. 2. It is easy to see that $O(\log(T))$ disks are needed. From Lemma 3.4, it follows that $O(\log(1/\epsilon) \cdot \log(T))$ poles are sufficient to approximate the nonreflecting boundary kernel on the line $\mathrm{Re}(z) = 1/T$.

Remark 3.3. A more careful analysis shows that $O(\log(1/\epsilon) + \log(T))$ poles actually suffice.

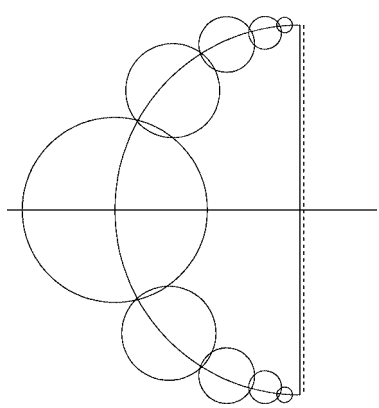

FIG. 2. A covering of the semicircle representing a continuous distribution of poles for the plane kernel. We carry out the Laplace transform on the dashed line $\mathrm{Re}(z) = 1/T$.

While the estimates above give a good asymptotic performance, in practice we reduce the constants with a somewhat different mechanism for obtaining pole approximations. Lemma 3.3 shows that it suffices to approximate the Laplace transforms of the kernels on the line $\mathrm{Re}(s) = 0$ where possible, and the line $\mathrm{Re}(s) = \eta = 1/T$ otherwise, with the relative error measured in the maximum norm. Nevertheless, we look for optimal rational approximations in weighted L_2 norms, using least-squares methods, where the weights are chosen to give small relative errors in the maximum norm.

Remark 3.4. Equation (16) shows that the plane kernel $\tilde{\tau}_w$ is a simple rescaling of $\tilde{\tau}_1$. Nevertheless, our ability to approximate $\tilde{\tau}_1$ only on $\mathrm{Re}(s) = \eta > 0$ limits the validity of a single approximation of $\tilde{\tau}_1$, rescaled for $\tilde{\tau}_w$, to a maximum value of w, and a maximum number of discrete modes.

3.2. Rational Approximation Technique

The (nonlinear) least-squares problem we choose to solve takes the form

$$\min_{P,Q} \int_{-\infty}^{\infty} \left| \frac{P(s)}{Q(s)} - \tilde{u}_v(s) \right|^2 ds \tag{19}$$

for P, Q polynomials with $\deg(P) + 1 = \deg(Q) = d$. Problem (19) is not only nonlinear, it is also very poorly conditioned when P, Q are represented in terms of their monomial coefficients. We apply two tactics for coping with these difficulties: linearization and orthogonalization.

We linearize the problem by starting with a good estimate of Q, and updating P, Q iteratively. In particular, we solve the linear least-squares problem

$$\min_{P^{(i+1)},Q^{(i+1)}} \int_{-\infty}^{\infty} \left| \frac{P^{(i+1)}(s)}{Q^{(i)}(s)} - \frac{Q^{(i+1)}(s)}{Q^{(i)}(s)} \tilde{u}_v(s) \right|^2 ds, \tag{20}$$

where the integral is replaced by a quadrature. The initial values $P^{(0)}$, $Q^{(0)}$ are obtained by exploiting the asymptotic expansion of the kernel at both zero and infinity.

The initialization for the plane boundary proceeds according to a simple recurrence. (The other boundaries, treated similarly, have recurrences originating with the Bessel functions, as presented in our earlier work [3].) Given the degree d, the kernel $\tau = \sqrt{s^2 + 1} - s$ is approximated by $P^{(0)}/Q^{(0)}$ computed by the following procedure:

$$\begin{aligned}
&(p, q) \leftarrow (0, 1)\\
&\text{do}\\
&\quad (p, q) \leftarrow (p(1 - s) + q,\ p + (1 + s)q) \qquad (21)\\
&\quad \text{if } \deg(q) = d \text{ then exit}\\
&\quad (p, q) \leftarrow (q/2,\ p/2 + s\,q) \qquad (22)\\
&\quad \text{if } \deg(q) = d \text{ then exit}\\
&\text{end}\\
&\left(P^{(0)}, Q^{(0)}\right) \leftarrow (p, q)
\end{aligned}$$

At each execution of (21), the approximation p/q agrees with τ to two more derivatives at $s = 0$; at each execution of (22), p/q agrees with τ to two orders higher at $s \to \infty$. The

execution of either (21) or (22) preserves the approximation order at the other point and increases the degree of p and q by 1.

The procedure to represent $P^{(i)}$, $Q^{(i)}$ and solve (20) is a fairly straightforward application of Gram–Schmidt orthogonalization. The cost of each linear least-squares solve is proportional to d^3; we have observed convergence for the nonlinear problem in two to four iterations. More details of the orthogonalization are presented in [3]. Since we are interested in using the results obtained there, we simply state as a theorem the outcome of the optimization process.

THEOREM 3.1 (Alpert *et al.* [3]). *The nonreflecting boundary kernels* $\sigma_{n,0}(t)$, $n > 0$, *and* $\omega_n(t)$ *can be represented for* $t \geq 0$ *with accuracy* ϵ *using* $O(\log n \log \frac{1}{\epsilon} + \log^2 \frac{1}{\epsilon})$ *poles in the Laplace domain. Kernel* $\sigma_{0,0}(t)$ *can be represented for* $0 \leq t \leq T$ *with* $O(\log T \log \frac{1}{\epsilon} + \log \frac{1}{\epsilon} \log\log \frac{1}{\epsilon} + \log T \log\log \frac{1}{\epsilon})$ *poles. Thus, in the time domain, they can be represented with the same number of decaying exponentials. The efficiency of the representation is indicated in Table I.* (*For* 15*-digit accuracy, about twice as many terms are required.*)

Remark 3.5. The use of poles (rational functions) in the Laplace domain and decaying exponentials in the time domain is a central topic in linear systems analysis and model

TABLE I

Number N of Poles Needed to Represent the Laplace Transform of the Nonreflecting Boundary Kernels $\sigma_{n,0}$, ω_n, and τ_w for $\epsilon = 10^{-8}$

$\sigma_{n,0}$		ω_n	
n	N	n	N
0	44		
1	15		
2	9		
3–8	7	0–7	n
9–10	8	8–10	8
11–14	9	11–14	9
15–20	10	15–19	10
21–28	11	20–28	11
29–41	12	29–40	12
42–58	13	41–57	13
59–84	14	58–83	14
85–123	15	84–123	15
124–183	16	124–183	16
184–275	17	184–275	17
276–418	18	276–418	18
419–638	19	419–637	19
639–971	20	638–971	20
972–1024	21	972–1024	21

Note. $\sigma_{n,0}$ is used for a circular boundary in two dimensions, ω_n is used for a spherical boundary in three dimensions, and τ_w is used for a planar boundary. (The data for $\sigma_{n,0}$ and ω_n are taken from [3]. For the plane kernel τ_w, a single representation of 64 poles suffices for all modes $n = 0, \ldots, 1024$ for $T < 10{,}000$.)

order reduction in electrical engineering and control theory [40, 42]. The compression techniques developed there are, of course, much more general than the one developed here. Unfortunately, the existing tools encounter serious instabilities in the present setting, while the approach outlined above is robust.

Remark 3.6. Although the cost of obtaining a kernel representation of size d is proportional to d^3, d grows only logarithmically in the wave problem size. In addition, the kernel representations are problem independent and can be computed once for all problems less than a particular size. We have computed and stored the representations needed for problems up to a rather large size.

4. DISCRETIZATION

Let us consider the wave equation (1) with $c = 1$ in the half-space $x > 0$ on a uniform Cartesian mesh with a nonreflecting boundary at $x = 0$. At all interior grid points, we obtain a second-order-accurate method using the usual central difference approximation:

$$\begin{aligned} &u(x, y, t + \lambda h) - 2u(x, y, t) + u(x, y, t - \lambda h) \\ &\quad = \lambda^2(u(x + h, y, t) + u(x, y + h, t) - 4u(x, y, t) + u(x - h, y, t) + u(x, y - h, t)). \end{aligned}$$

Note that we have fixed $\delta x = \delta y = h, \delta t = \lambda h$. For higher order accuracy, we follow the Lax–Wendroff approach. For example, beginning with the Taylor expansion

$$\frac{u(t + \delta t) - 2u(t) + u(t - \delta t)}{\delta t^2} = u_{tt}(t) + \frac{\delta t^2}{12} u_{tttt}(t) + O(\delta t^4),$$

we use the wave equation $u_{tt} = \Delta u$ to obtain

$$\frac{u(t + \delta t) - 2u(t) + u(t - \delta t)}{\delta t^2} = \Delta u(t) + \frac{\delta t^2}{12} \Delta^2 u(t) + O(\delta t^4).$$

This allows us to exchange high-order temporal differentiation and the accompanying storage requirements for spatial differences. By approximating the Laplacian to fourth order (using a standard nine-point stencil) and the biharmonic operator to second order, we maintain the fourth-order accuracy. For grid points near the boundary, we use standard one-sided finite differences to obtain fourth-order accuracy. Beyond fourth order, instabilities arise from the use of one-sided differences on a uniform mesh. This is remedied by modifying the mesh near boundaries. In particular, the eighth-order discretization used to obtain some of the results below employs Alpert's eighth-order Gauss-trapezoidal quadrature mesh [2]. Here the points h and $2h$ on the uniform mesh are replaced by three points, approximately $0.21h$, $0.98h$, and $1.99h$. See [24] for more details.

Our implementations of the nonreflecting boundary condition (6) are a bit more involved. At $x = 0$, we need to enforce the equation

$$\hat{u}_x(x, \eta, \zeta, t) + \hat{u}_t(x, \eta, \zeta, t) + [\tau_w * \hat{u}](x, \eta, \zeta, t) = 0. \tag{23}$$

For some of our experiments, we apply this condition at staggered points in time. That is,

for second-order accuracy, we use the approximations

$$\hat{u}_x(0,\eta,\zeta,t+h/2) = \frac{1}{2}\left[\delta_x^{(2)}\hat{u}(0,\eta,\zeta,t+h) + \delta_x^{(2)}\hat{u}(0,\eta,\zeta,t)\right] + O(h^2)$$
$$\hat{u}_t(0,\eta,\zeta,t+h/2) = \frac{\hat{u}(0,\eta,\zeta,t+h) - \hat{u}(0,\eta,\zeta,t)}{h} + O(h^2),$$

where $\delta_x^{(2)}\hat{u}(0,\eta,\zeta,t)$ denotes the second-order one-sided three-point approximation to the x-derivative. We then replace (23) with a discrete version,

$$\frac{1}{2}\left[\delta_x^{(2)}\hat{u}(0,\eta,\zeta,t+h) + \delta_x^{(2)}\hat{u}(0,\eta,\zeta,t)\right] + \frac{\hat{u}(0,\eta,\zeta,t+h) - \hat{u}(0,\eta,\zeta,t)}{h} + [\tau_w * \hat{u}](0,\eta,\zeta,t+h/2) = 0, \tag{24}$$

where the convolution integral $[\tau_w * \hat{u}](0,\eta,\zeta,t+h/2)$ is computed using the midpoint rule. In order to be efficient, of course, we use the recurrence relation of Lemma 3.2 to eliminate the burden of history dependence.

For fourth-order accuracy, we use a Taylor expansion in time and the Lax–Wendroff technique to obtain

$$\hat{u}_x(0,\eta,\zeta,t+h/2) = \frac{1}{2}\left[\delta_x^{(4)}\hat{u}(0,\eta,\zeta,t+h) + \delta_x^{(4)}\hat{u}(0,\eta,\zeta,t)\right] + \frac{h^2}{16}[\Delta\hat{u}_x(0,\eta,\zeta,t+h) + \Delta\hat{u}_x(0,\eta,\zeta,t)] + O(h^4),$$
$$\hat{u}_t(0,\eta,\zeta,t+h/2) = \frac{\hat{u}(0,\eta,\zeta,t+h) - \hat{u}(0,\eta,\zeta,t)}{h} + \frac{h^2}{24}\left[\frac{\Delta_h\hat{u}(0,\eta,\zeta,t+h) - \Delta_h\hat{u}(0,\eta,\zeta,t)}{h}\right] + O(h^4),$$

where $\delta_x^{(4)}\hat{u}(0,\eta,\zeta,t)$ denotes the fourth-order, one-sided, five-point approximation to the x-derivative and $\Delta_h\hat{u}(0,\eta,\zeta,t)$ is a second-order-accurate approximation of the Laplacian.

We are still working in the Fourier domain, so that

$$\Delta_h\hat{u}(0,\eta,\zeta,t) = \delta_{xx}^{(2)}\hat{u}(0,\eta,\zeta,t) - (\eta^2+\zeta^2)\hat{u}(0,\eta,\zeta,t),$$

where $\delta_{xx}^{(2)}\hat{u}(0,\eta,\zeta,t)$ is a one-sided, second-order-accurate approximation of the second derivative. A second-order-accurate stencil for $\Delta\hat{u}_x(0,\eta,\zeta,t)$ is obtained using a one-sided, five-point approximation. Equation (23) is then replaced with

$$\frac{1}{2}\left[\delta_x^{(4)}\hat{u}(0,\eta,\zeta,t+h) + \delta_x^{(4)}\hat{u}(0,\eta,\zeta,t)\right] + \frac{h^2}{16}[\Delta\hat{u}_x(0,\eta,\zeta,t+h) + \Delta\hat{u}_x(0,\eta,\zeta,t)] + \frac{\hat{u}(0,\eta,\zeta,t+h) - \hat{u}(0,\eta,\zeta,t)}{h} + \frac{h^2}{24}\frac{\Delta_h\hat{u}(0,\eta,\zeta,t+h) - \Delta_h\hat{u}(0,\eta,\zeta,t)}{h} + [\tau_w * \hat{u}](0,\eta,\zeta,t+h/2) = 0. \tag{25}$$

Our eighth-order implementation uses similar ideas. Even-order time derivatives of u are obtained from the interior, and odd-order derivatives from the boundary condition. The latter is applied not only to u, but also to the even-order time derivatives of u. The convolution is computed in differential form using implicit Adams methods.

Remark 4.1. The second- and fourth-order marching schemes, (24) and (25), as well as the Adams methods used at eighth order, are implicit. Since the modes (indexed by η and ζ) are uncoupled, however, their solution is trivial, involving only a scalar division.

Remark 4.2. For a spherical boundary, it is necessary to efficiently compute the spherical harmonic transforms and their inverses. Despite recent advances on this problem [26], we use the standard method [19]. For the waveguide problem below, we discretize the Fourier integrals using the Gauss-trapezoidal rule [2]. As this reduces to the standard discrete Fourier transform plus a couple of terms, the FFT can still be used.

5. NUMERICAL RESULTS

We introduce several model problems to compare our implementation of the nonreflecting boundary conditions to other methods and to exact solutions. To distinguish spatiotemporal discretization errors from those due to the implementation of nonreflecting boundary conditions, we perform some duplicate computations employing exact Dirichlet boundary conditions and thereby estimate the error due to discretization alone.

5.1. Rectangle

We consider first a rectangular domain $(x, y) \in (-1, 1) \times (0, 1)$, with periodic boundary conditions at $y = 0, 1$. The field arises from point sources at

$$\{(x_k, y_k) = (0, k + 1/2) \mid k \in \mathbb{Z}\}, \tag{26}$$

with the excitation of every source given by $f(t) = e^{-\alpha(t-\tau)^2}$, with $\alpha = 150$ and $\tau = -0.5$. The exact solution is

$$u(x, y, t) = \sum_{k=-\infty}^{\infty} \int_{-\infty}^{t-r_k} \frac{f(s)}{\sqrt{(t-s)^2 - r_k^2}}\, ds, \tag{27}$$

where $r_k^2 = x^2 + (y - y_k)^2$. Note that $f(t)$ is negligible for $t \geq 0$, and $u(\pm 1, y, 0)$ and $u_t(\pm 1, y, 0)$ are also negligible (by the start time, the sources are off and the waves have not yet reached the boundary). The solution is evaluated via a combination of Gauss–Legendre and endpoint-corrected trapezoidal rules to an accuracy of at least 10^{-9}. Shown in Fig. 3, it has a steady stream of waves arriving from ever more distant sources, and the amplitudes of these waves decay rather slowly in time. Containing both very low frequencies and glancing angles, the waves represent a significant challenge for nonreflecting boundary conditions.

For the numerical study, we begin with the solution at times $t = 0$ and $t = \delta t$, and evolve for $t \in [0, 50]$ using the fourth-order-accurate discretizations described in Section 4. We choose node spacing h in x and y, for $h = 1/25$, $1/50$, and $1/100$, with time steps defined by $\lambda = 1/2, 5/8$.

For both second- and fourth-order implementations, the spatially global relative l_2-error conforms to $O(h^p)$, where p is the order. In Table II we show the error of the computed solution for the fourth-order method, comparing exact Dirichlet boundary conditions and the exact nonreflecting boundary conditions. We represent the plane nonreflecting boundary kernel with a 21-pole approximation, for which $\eta = 1/T = 10^{-4}$ and $\epsilon = 9.8 \times 10^{-5}$ (see Section 3.1).

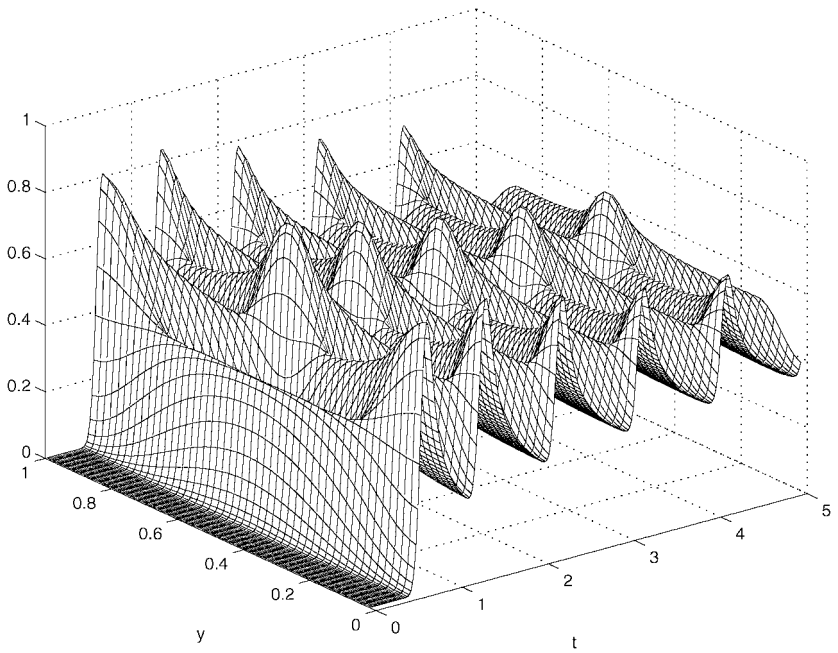

FIG. 3. Waves due to a periodically repeated source impinging on the $x = 1$ boundary of the rectangular domain (exact solution).

For purposes of comparison, we solved the same problem using a strongly well-posed perfectly matched layer (PML). Introduced for Maxwell's equations by Berenger [7] in 1994, the PML seems to have become the method of choice in computational electromagnetics. It improves on earlier absorbing layers (for example [27]) by having a reflectionless interface with the physical domain. The original formulation applies only to the Maxwell system and is only weakly well posed. Later formulations by Collino and Monk [8] and Petropoulos [33] are mathematically cleaner. We use them as the basis of our layer construction for the wave equation.

As discussed in [23], an integral formulation of reflectionless absorbing layers for the wave equation is given by

$$u_{tt} = (1 - \sigma(x)\mathcal{I}*)((1 - \sigma(x)\mathcal{I}*)u_x)_x + u_{yy}, \tag{28}$$

$$\mathcal{I} * \phi = \int_0^t e^{-\sigma(x)(t-\tau)}\phi(\tau)\, d\tau. \tag{29}$$

TABLE II
For Rectangle, Maximum Errors of Fourth-Order Code, $0 \le t \le 50$

Boundary treatment	$h = 1/25$	$h = 1/50$	$h = 1/100$
Exact Dirichlet	6.0×10^{-2}	7.3×10^{-3}	5.0×10^{-4}
21-Pole NRBC	3.8×10^{-2}	6.7×10^{-3}	4.2×10^{-4}

Here, $\sigma(x)$ is a nonnegative function. Obviously, the layer equation reduces to the wave equation when $\sigma = 0$. The equation is then recast into differential form via the introduction of auxiliary variables. The latter step may be accomplished in a number of distinct ways. For the rectangle experiments we write

$$\frac{\partial^2 u}{\partial t^2} = c^2\left(\nabla^2 u - \frac{\partial v}{\partial x} - w\right), \tag{30}$$

$$\frac{\partial v}{\partial t} + \sigma(x)v = \sigma(x)\frac{\partial u}{\partial x}, \tag{31}$$

$$\frac{\partial w}{\partial t} + \sigma(x)w = \sigma(x)\frac{\partial^2 u}{\partial x^2} - \sigma(x)\frac{\partial v}{\partial x}. \tag{32}$$

The layers have width d and thus comprise the intervals $x \in (1, 1+d) \cup (-1-d, -1)$. They are terminated with the simple periodic boundary conditions; that is, the right boundary $1 + d$ is identified with the left boundary, $-1 - d$. We use a quartic absorption profile,

$$\sigma(x) = \sigma_m\left(\frac{x-1}{d}\right)^4, \quad x \in (1, 1+d), \tag{33}$$

analogously defined on the left.

To discretize the u equation we essentially follow the same strategy as in the interior. We also obtain first-order derivative terms in time for u which we discretize one sided and correct to higher order using spatial derivatives. The final formulas in time are given by

$$\begin{aligned}
&\frac{u(t+\delta t) - 2u(t) + u(t-\delta t)}{\delta t^2} \\
&\quad = \Delta u(t) - v_x(t) - w(t) + \frac{\delta t^2}{12}\Delta^2 u(t) + \frac{\delta t^2}{4}\sigma(\sigma(u_x(t) - v(t)))_x \\
&\qquad - \frac{\delta t^2}{12}(\Delta(v_x(t) + w(t)) + \sigma^2 w(t)) - \frac{\delta t^3}{12}\sigma'(u_x(t) - u_x(t-\delta t)) \\
&\qquad - \frac{\delta t^3}{6}\sigma(u_{xx}(t) - u_{xx}(t-\delta t)) - \frac{\delta t^5}{12}\sigma\Delta u_{xx}(t) - \frac{\delta t^5}{24}\sigma'\Delta u_x(t) \\
&\qquad + \frac{\delta t^5}{12}\sigma(v_{xxx}(t) + w_{xx}(t)) + \frac{\delta t^5}{24}\sigma'(v_{xx}(t) + w_x(t)).
\end{aligned} \tag{34}$$

For the auxiliary equations we make an exponential transformation,

$$v = e^{-\sigma(t-t_n)}\bar{v}, \quad w = e^{-\sigma(t-t_n)}\bar{w}, \tag{35}$$

at each time step. The equations for the barred variables are discretized directly using Simpson's rule. Note that this involves no additional implicit calculations, as we sequentially update u, then v, then w. The final formulas are

$$v(t+\delta t) = e^{-2\sigma\delta t}v(t-\delta t) + \frac{\delta t}{3}(\sigma u_x(t+\delta t) + 4\sigma e^{-\sigma\delta t}u_x(t) + \sigma e^{-2\sigma\delta t}u_x(t-\delta t)), \tag{36}$$

$$\begin{aligned}
w(t+\delta t) = e^{-2\sigma\delta t}w(t-\delta t) + \frac{\delta t}{3}[&\sigma(u_{xx}(t+\delta t) - v_x(t+\delta t)) + 4\sigma e^{-\sigma\delta t}(u_{xx}(t) - v_x(t)) \\
&+ \sigma e^{-2\sigma\delta t}(u_{xx}(t-\delta t) - v_x(t-\delta t))].
\end{aligned} \tag{37}$$

TABLE III
Maximum Errors for Rectangle as a Function of σ_m ($d = 1$)

σ_m	10	20	30	40	50
Max. err.	1.0×10^{-1}	8.8×10^{-2}	1.1×10^{-1}	1.7×10^{-1}	2.4×10^{-1}

Recalling the continuity of the fields and their first four derivatives across the interface and the periodic boundary conditions, we see that no special one-sided spatial derivative formulas are needed. Therefore, we use a uniform mesh and central differences everywhere, choosing their order to maintain overall fourth-order accuracy.

We present tests for three values of d, $d = 0.5, 1, 1.5$. In each case we tried a range of values for σ_m between 10 and 50 in steps of 10. In Table III we illustrate the effect of changing σ_m on the maximum error.

In Table IV we present some time history of the errors computed with $h = 1/100$, $\lambda = 0.5$. For the PML the results shown are for the best choice of σ_m tested. We also list the errors obtained using exact Dirichlet conditions to assess the effect of discretization error. Note that the times shown in the table are rather coarsely spaced so that maximum errors listed earlier, which come from measurements on 500 time intervals, may be larger by factors of up to 3.

We see that the computations using the compressed kernel are essentially as accurate as those using the exact Dirichlet conditions. For the PML we require at least $d = 1$ to get any accuracy for long time; that is, we need layers with at least 100 points.

TABLE IV
Errors for Various Boundary Treatments on Rectangle, $h = 1/100$

Time	Exact	21-Pole	$d = 0.5$	$d = 1$	$d = 1.5$
2.5	0.00008	0.00008	0.08144	0.00045	0.00009
5.0	0.00013	0.00012	0.11047	0.00527	0.00016
7.5	0.00020	0.00016	0.13866	0.00957	0.00034
10.0	0.00024	0.00020	0.13796	0.02189	0.00093
12.5	0.00027	0.00023	0.13483	0.02440	0.00205
15.0	0.00028	0.00025	0.13956	0.02569	0.00311
17.5	0.00029	0.00027	0.14883	0.02685	0.00446
20.0	0.00031	0.00029	0.15732	0.02789	0.00623
22.5	0.00032	0.00030	0.16681	0.02959	0.00817
25.0	0.00032	0.00032	0.17909	0.03106	0.01018
27.5	0.00032	0.00033	0.19395	0.03191	0.01222
30.0	0.00032	0.00034	0.21018	0.03235	0.01426
32.5	0.00031	0.00035	0.22822	0.03273	0.01627
35.0	0.00032	0.00036	0.24816	0.03335	0.01824
37.5	0.00030	0.00037	0.27018	0.03435	0.02018
40.0	0.00029	0.00038	0.29450	0.03566	0.02210
42.5	0.00030	0.00039	0.32054	0.03730	0.02402
45.0	0.00029	0.00040	0.34815	0.03933	0.02595
47.5	0.00028	0.00041	0.37754	0.04175	0.02791
50.0	0.00028	0.00041	0.40903	0.04453	0.02990

5.2. Waveguide

We consider next the Cauchy problem in an infinite, two-dimensional waveguide, $(x, y) \in (-\infty, \infty) \times (0, 1)$, with homogeneous Neumann boundary conditions imposed on the walls:

$$u(x, y, 0) = u_0(x, y), \quad u_t(x, y, 0) = v_0(x, y), \tag{38}$$

$$u_y(x, y, t) = 0, \quad y = 0, 1. \tag{39}$$

We choose initial data supported in $x \in (-2, 2)$ such that the exact solution can be evaluated to high accuracy. Precisely, $u(x, y, t)$ is also given by (27) with $\alpha = 30, \tau = -0.95$, and $y_0 = 1/3$. The remaining y_k, all outside $[0, 1]$, are chosen so that the boundary condition is satisfied. The first few are given by

$$y_1 = 5/3, \quad y_{-1} = -1/3, \quad y_2 = 7/3, \quad y_{-2} = -5/3, \tag{40}$$

with the general rule ($k \geq 0$)

$$y_{k+1} = 2 - y_{-k}, \quad y_{-(k+1)} = -y_k. \tag{41}$$

For reference we give in Fig. 4 contour plots of the solution at times 1, 2, 5, 10, 25, 50. It should be noted that as time progresses waves are incident on the artificial boundary at glancing angles, which is generally the most difficult case for low-order boundary conditions and sponge layers to handle.

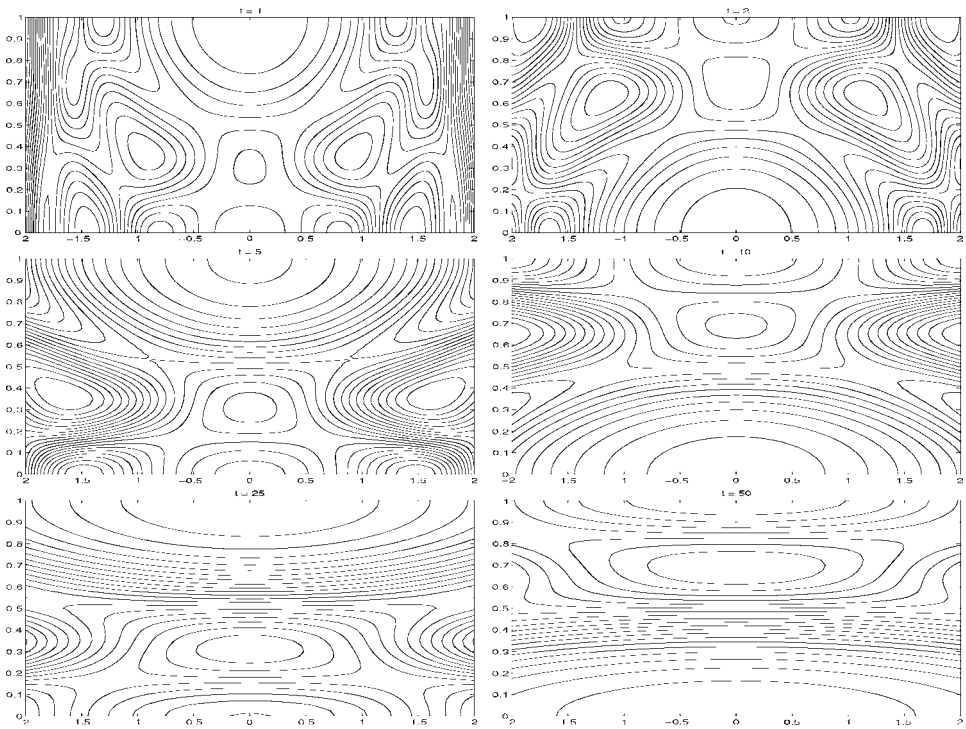

FIG. 4. Contours of the exact solution for the waveguide at various times.

TABLE V
For Waveguide, Maximum Errors $0 \le t \le 50$

Poles	Modes	$h = 1/32$	$h = 1/64$	$h = 1/128$
0	—	1.1×10^{-1}	1.1×10^{-1}	1.1×10^{-1}
21	4	5.0×10^{-3}	4.9×10^{-3}	4.9×10^{-3}
21	8	5.3×10^{-5}	5.1×10^{-5}	5.1×10^{-5}
21	16	6.1×10^{-5}	4.0×10^{-6}	4.0×10^{-6}
21	32	—	4.0×10^{-5}	4.0×10^{-6}
21	48	—	1.5×10^{-2}	4.0×10^{-6}
31	4	5.0×10^{-3}	4.9×10^{-3}	4.9×10^{-3}
31	8	5.3×10^{-5}	5.1×10^{-5}	5.0×10^{-5}
31	16	4.4×10^{-5}	5.5×10^{-8}	3.2×10^{-8}
31	32	—	4.0×10^{-5}	3.2×10^{-8}
31	48	—	1.5×10^{-2}	1.2×10^{-6}

We consider two different collections of poles to approximate the plane kernel: a 21-pole compression following from the parameters $\eta = 10^{-4}, \epsilon = 10^{-4}$, and a 31-pole compression computed with $\eta = 10^{-4}, \epsilon = 10^{-6}$. Note that the exact solution is $O(1)$, so that the absolute errors (shown in Tables V–VII) are the same order of magnitude as the relative errors.

5.2.1. *High-Order Results*

We begin by demonstrating the accuracy attainable using the rational approximants of the nonreflecting boundary kernels and an eighth-order-accurate discretization. We first consider the maximum l_2-error on the mesh for times up to 50 for various meshes and numbers of modes used in the boundary condition. In Table V we compare the 21- and 31-pole computations and, for reference, a computation using the simple Sommerfeld condition. (The latter may be thought of as a 0-pole approximation.)

The data paint a clear picture. First of all, the Sommerfeld condition is quite inaccurate over long time, independent of the mesh. Second, on fixing the mesh, the error at first decreases as the number of modes in the boundary condition is increased, but then it grows. The latter effect is due to errors in computing the Fourier integrals. The 31-pole compression is clearly more accurate than the 21-pole compression and provides nearly the maximal attainable accuracy with 16 modes on the finest mesh. For each of these, we are able to attain more accuracy than guaranteed by the choice of ϵ.

It is also of interest to look at the time dependence of the errors, shown in Table VI. Here we consider our coarsest mesh, $h = 1/32$, and use 16 modes. In general, we observe a growth of error in time for the uniform approximants, while the error for the Sommerfeld condition peaks at $t = 25$ and remains at roughly the same level thereafter.

5.2.2. *Comparisons with Other Methods*

For purposes of comparison, we have also implemented a PML and the second-order Engquist–Majda condition [10]:

$$u_{tt} \pm u_{xt} - \frac{1}{2} u_{yy} = 0. \tag{42}$$

TABLE VI
Time History of Errors for Waveguide: $h = 1/32$, 16 modes

Time	Sommerfeld	21-Pole	31-Pole
2.5	1.7×10^{-2}	4.3×10^{-6}	3.5×10^{-6}
5.0	4.6×10^{-2}	6.1×10^{-6}	4.2×10^{-6}
7.5	6.5×10^{-2}	7.6×10^{-6}	5.6×10^{-6}
10.0	6.9×10^{-2}	1.1×10^{-5}	7.7×10^{-6}
12.5	4.8×10^{-2}	1.4×10^{-5}	1.0×10^{-5}
15.0	7.0×10^{-2}	1.6×10^{-5}	1.2×10^{-5}
17.5	6.7×10^{-2}	2.0×10^{-5}	1.4×10^{-5}
20.0	6.1×10^{-2}	2.2×10^{-5}	1.6×10^{-5}
22.5	9.7×10^{-2}	2.6×10^{-5}	1.9×10^{-5}
25.0	4.6×10^{-2}	2.8×10^{-5}	2.0×10^{-5}
27.5	1.1×10^{-1}	3.3×10^{-5}	2.4×10^{-5}
30.0	4.3×10^{-2}	3.5×10^{-5}	2.5×10^{-5}
32.5	1.1×10^{-1}	3.9×10^{-5}	2.8×10^{-5}
35.0	5.5×10^{-2}	4.1×10^{-5}	2.9×10^{-5}
37.5	9.7×10^{-2}	4.6×10^{-5}	3.3×10^{-5}
40.0	7.0×10^{-2}	4.7×10^{-5}	3.4×10^{-5}
42.5	8.4×10^{-2}	5.2×10^{-5}	3.8×10^{-5}
45.0	7.6×10^{-2}	5.4×10^{-5}	3.8×10^{-5}
47.5	6.5×10^{-2}	5.9×10^{-5}	4.2×10^{-5}
50.0	7.8×10^{-2}	6.0×10^{-5}	4.3×10^{-5}

As these implementations are only second order, we repeat our computations with the 21-pole compression using the second-order method. It should be noted that even on the finest mesh we found it feasible to use routinely, 512×128, the long time accuracy using exact Dirichlet boundary data is modest—a maximum error of 4.2×10^{-3}. In Table VIII we include the errors using exact Dirichlet boundary conditions for clarity.

For these experiments we used a slightly different set of auxiliary variables within the PML. Precisely we set

$$v_t + \sigma v = u_x, \tag{43}$$

$$w_{tt} + 2\sigma w_t + \sigma^2 w = u_{xx} - \sigma' v. \tag{44}$$

We then have

$$u_{tt} = u_{xx} + u_{yy} - 2\sigma w_t - \sigma^2 w - \sigma' v. \tag{45}$$

Equation (45) is discretized by central differences analogous to our discretization of the wave equation itself. Our discretization of the evolution equations for the auxiliary variables w and v was derived by the same methods leading to (36) and (37) except that only second-order accuracy was required. This results in the formulas

$$\begin{aligned} w(x, y, t + \delta t) = {} & e^{-\sigma(x)\delta t}(2w(x, y, t) - \lambda^2 h^2 \sigma'(x) v(x, y, t)) - e^{-2\sigma(x)\delta t} w(x, y, t - \delta t) \\ & + \lambda^2 e^{-\sigma(x)\delta t}[u(x + h, y, t) - 2u(x, y, t) + u(x - h, y, t)], \end{aligned} \tag{46}$$

$$v(x, y, t + \delta t) = e^{-2\sigma(x)\delta t} v(x, y, t - \delta t) + \lambda e^{-\sigma(x)\delta t}[u(x + h, y, t) - u(x - h, y, t)]. \tag{47}$$

TABLE VII
Maximum Errors for Waveguide as a Function of σ_m ($d = 1$)

σ_m	4	6	8	10	12	15
Max. err.	5.8×10^{-2}	4.3×10^{-2}	4.3×10^{-2}	5.2×10^{-2}	6.8×10^{-2}	1.0×10^{-1}

A single layer was attached to the computational domain, with periodic boundary conditions imposed. The absorption profile $\sigma(x)$ was chosen to vanish along with its first derivative at the interface with the physical domain and to be continuously differentiable at the periodic boundary. It is characterized by two parameters, the width d and maximum absorption σ_m, and is given by

$$\sigma = \begin{cases} \sigma_m \cdot \frac{(x-2)^2}{d^2} \cdot \frac{(2+2d-x)^2}{d^2}, & x \in (2, 2+d); \\ \sigma_m \cdot \frac{(2+x)^2}{d^2} \cdot \frac{(2+2d+x)^2}{d^2}, & x \in (-2-d, -2). \end{cases} \tag{48}$$

We tested $d = 0.75, 1, 1.5, 2, 3$. In each case σ_m was roughly chosen to minimize the maximum error. For example, for $d = 1$ we obtained the maximum errors shown in Table VII.

In Table VIII we show the evolution for nine cases—exact Dirichlet data (to assess the effects of discretization error), our 21-pole, 16-mode compression of the exact condition, the PML for the five widths considered, and finally local radiation boundary conditions, including the simple Sommerfeld condition and the second-order Engquist–Majda condition (42), labeled EM1 and EM2.

TABLE VIII
Errors for Various Boundary Treatments for Waveguide, Second Order, $h = 1/128$

Time	Exact	21-Pole	$d = 0.75$	$d = 1$	$d = 1.5$	$d = 2$	$d = 3$	EM1	EM2
2.5	0.0005	0.0004	0.0004	0.0004	0.0004	0.0004	0.0004	0.0151	0.0038
5.0	0.0008	0.0007	0.0020	0.0016	0.0008	0.0007	0.0007	0.0438	0.0135
7.5	0.0009	0.0008	0.0043	0.0038	0.0009	0.0008	0.0008	0.0630	0.0289
10.0	0.0014	0.0012	0.0081	0.0070	0.0012	0.0012	0.0012	0.0653	0.0333
12.5	0.0011	0.0010	0.0113	0.0084	0.0010	0.0010	0.0010	0.0457	0.0322
15.0	0.0019	0.0016	0.0130	0.0101	0.0016	0.0015	0.0015	0.0664	0.0367
17.5	0.0016	0.0011	0.0152	0.0122	0.0016	0.0012	0.0011	0.0637	0.0465
20.0	0.0023	0.0019	0.0222	0.0189	0.0027	0.0019	0.0018	0.0587	0.0320
22.5	0.0016	0.0013	0.0222	0.0152	0.0032	0.0015	0.0013	0.0936	0.0642
25.0	0.0026	0.0021	0.0258	0.0223	0.0044	0.0024	0.0021	0.0435	0.0266
27.5	0.0027	0.0014	0.0274	0.0205	0.0056	0.0022	0.0014	0.1026	0.0684
30.0	0.0028	0.0024	0.0311	0.0247	0.0067	0.0031	0.0023	0.0402	0.0293
32.5	0.0024	0.0016	0.0371	0.0234	0.0086	0.0033	0.0016	0.1029	0.0681
35.0	0.0031	0.0026	0.0346	0.0271	0.0094	0.0041	0.0026	0.0496	0.0340
37.5	0.0026	0.0017	0.0473	0.0297	0.0120	0.0047	0.0018	0.0936	0.0648
40.0	0.0031	0.0028	0.0408	0.0268	0.0129	0.0052	0.0030	0.0632	0.0389
42.5	0.0029	0.0019	0.0560	0.0366	0.0158	0.0065	0.0020	0.0799	0.0595
45.0	0.0032	0.0030	0.0496	0.0272	0.0170	0.0063	0.0034	0.0689	0.0417
47.5	0.0033	0.0020	0.0648	0.0414	0.0202	0.0084	0.0025	0.0616	0.0527
50.0	0.0032	0.0032	0.0600	0.0296	0.0214	0.0079	0.0038	0.0708	0.0431

TABLE IX
Parameters for the Waveguide Timing Tests

Case	Time	Tolerance	Spatial mesh	PML width (each side)
1	25	0.01	200×50	2.6
2	50	0.01	260×65	3.69
3	10	0.001	560×140	1.5
4	25	0.001	760×190	3.0
5	50	0.001	880×220	5.11

We see that both our 21-pole compression and the PML with $d = 3$ provide results as accurate as those obtained with exact Dirichlet data. That is, the errors associated with these domain truncations are dominated by the discretization error. However, it should be noted that the storage and computation costs associated with our compressed exact boundary condition are much smaller than those associated with a width 3 PML. We require 21×16 auxiliary variables at each boundary and an additional 256 variables used for the FFT. On the other hand, the PML uses $384 \times 128 \times 3$ variables in the layer—more than 200 times as many. For shorter time intervals and less stringent accuracy requirements this can certainly be decreased. For example, for $t \leq 10$ and an error tolerance of 10^{-2}, $d = 0.75$ suffices, but this is still significantly more costly than the nonreflecting boundary condition. We should also recall that our boundary condition is capable of providing errors smaller by orders of magnitude if high-order discretizations are used. The low-order local boundary conditions provide modest accuracy at best, with errors larger than 10^{-2} by $t = 5$.

5.2.3. *Timing Results*

To demonstrate the practical efficiency of the proposed boundary conditions in comparison with the PML for moderate accuracy requirements we conducted timing experiments with the waveguide problem (Tables IX and X). We considered solution times of $t = 10$, 25, 50 and error tolerances of 10^{-2} and 10^{-3} . In all cases we used standard second-order central differencing with a CFL number of $1/2$. We first carried out experiments using exact Dirichlet boundary conditions to determine the coarsest mesh for which the tolerances could be met. Our approximate boundary conditions used nine Fourier modes and the 21-pole approximation. Nine modes were more than sufficient in all cases to meet the accuracy requirements. Using so few modes and given the fact that the meshes were not chosen to optimize the efficiency of the FFT, we simply computed the transforms by direct integration and series summation. For the PML we experimentally minimized the layer width required, considering a number of different values for the absorption parameter. For the layer we implemented we are confident that we are within 5% of the minimum width.

TABLE X
Time in Seconds for the Waveguide Timing Tests with Various Boundary Treatments

Domain truncation	Case 1	Case 2	Case 3	Case 4	Case 5
Dirichlet	2	12	107	1010	3545
9-Mode, 21-pole BC	4	17	127	1013	3640
PML	31	334	427	7121	37314

The experiments were conducted on a computer with dual 400-MHz processors and 2 GB of memory. The Fortan 77 compiler was used with optimization enabled. For the short runs, the output of the time command was repeatable to within 1 s, and for the longer runs to within 5%. (In cases where multiple runs were made we report the first result.) In the final timing runs we suppressed all calls to the routines evaluating the exact solution, as they are quite expensive. For $t = 10$ and a tolerance of 10^{-2} all runs required less than 1 s, so that no comparison could be made. The results in the other five cases are tabulated below.

We begin with the obvious conclusion that the proposed boundary conditions are vastly more efficient than the PML in these experiments. Of course, a multitude of PML formulations have been proposed and others may be cheaper than the one we have used. However, it is clear that the new boundary conditions are insignificantly more expensive than simple Dirichlet conditions and provide excellent accuracy. Moreover, the necessary width for the PML is strongly dependent on time, as predicted for waveguide problems in [23]. We thus feel it is unlikely that any PML approach will be competitive with the proposed boundary conditions for any problem of this type. In addition we note that the advantage in using the nonreflecting boundary conditions is more pronounced for tighter error tolerances, and that we have neglected the significant efforts required to optimize the PML.

5.3. Annulus

We consider next the propagation of a pulse through an annular domain $(r, \theta) \in (0.8, 1) \times [0, 2\pi)$, with Dirichlet boundary condition at $r = 0.8$ and nonreflecting boundary at $r = 1$. The field arises from a single point source at $(r, \theta) = (0.7, 0)$ with excitation $f(t) = e^{-\alpha(t-\tau)^2}$, with $\alpha = 150$ and $\tau = 0.1$. The exact solution is computed as above for the rectangle or waveguide, except that a single source is present.

We compute the numerical solution with a second-order- and a fourth-order-accurate code, and rational approximations to the nonreflecting boundary kernels that are accurate to $\epsilon = 10^{-8}$. (The number of poles required is shown in Table I.) The discretizations are similar to those above for the rectangle, except that here we employ radial grids in place of Cartesian. In Table XI we show the global relative l_2-error on the annulus at various times for the two codes with three different discretization refinements. For this problem, we integrate only to time $t = 3$, for the impulse has largely left the domain by that time.

TABLE XI

Errors for Annulus with Nonreflecting Boundary, Second- and Fourth-Order Codes

	$\delta r = 1/40$ $\delta\theta = \pi/50$ $\delta t = 1/50$		$\delta r = 1/80$ $\delta\theta = \pi/100$ $\delta t = 1/100$		$\delta r = 1/160$ $\delta\theta = \pi/200$ $\delta t = 1/200$	
Time	2nd	4th	2nd	4th	2nd	4th
0.5	3.6×10^{-2}	2.3×10^{-2}	8.5×10^{-3}	1.1×10^{-3}	2.1×10^{-3}	6.7×10^{-5}
1.0	3.8×10^{-2}	1.8×10^{-2}	9.9×10^{-3}	1.1×10^{-3}	2.5×10^{-3}	7.4×10^{-5}
1.5	1.3×10^{-2}	1.3×10^{-2}	2.5×10^{-3}	3.0×10^{-4}	5.7×10^{-4}	2.0×10^{-5}
2.0	9.8×10^{-3}	3.6×10^{-2}	1.6×10^{-3}	9.7×10^{-4}	3.4×10^{-4}	4.2×10^{-5}
2.5	2.5×10^{-3}	1.7×10^{-2}	2.7×10^{-5}	2.9×10^{-5}	3.0×10^{-6}	2.3×10^{-7}
3.0	2.0×10^{-3}	1.6×10^{-2}	8.1×10^{-6}	1.1×10^{-6}	3.3×10^{-7}	8.8×10^{-8}

TABLE XII
Parameter Values of the Sources for the Field on the Sphere

			$\mathbf{p}_k$		
k	α_k	τ_k	x_k	y_k	z_k
1	100	0.5	0.5	0.8	0.0
2	100	0.6	0.0	0.5	0.8
3	100	0.7	0.8	0.0	0.5
4	100	0.8	0.8	0.5	0.0
5	100	0.9	0.0	0.8	0.5
6	100	1.0	0.5	0.0	0.8

5.4. Sphere

Our final numerical example is for a spherical boundary. The field is due to six Gaussian-excited point sources inside the sphere $r = 1$,

$$u(\mathbf{x}, t) = \sum_{k=1}^{6} \frac{e^{-\alpha_k (t-\tau_k-r_k)^2}}{r_k}, \tag{49}$$

where $r_k = \|\mathbf{x} - \mathbf{p}_k\|$. The values of α_k, τ_k, and $\mathbf{p}_k$ are given in Table XII.

Rather than integrate the fully three-dimensional problem, we defer the volume gridding issue by computing the time-dependent Dirichlet-to-Neumann map on the sphere itself. More precisely, we compute the radial derivative u_r from (12), where each wavenumber of the field at each time is obtained by a spherical–harmonic transformation applied to the exact field on an equiangular grid in spherical coordinates θ, ϕ. The time derivative of the field is obtained by finite differences, and the convolution integral is discretized by a quadrature, with equispaced times.

The convolution kernels are approximated to accuracy $\epsilon = 10^{-8}$, using the number of poles shown in Table I. We compute the time derivatives and convolution integrals to second-, fourth-, and eighth-order accuracy. Our spatial discretizations correspond to spherical–harmonic expansion triangular truncations of various orders N that are common in weather and climate simulators and use a reference spherical–harmonics transform implementation [19]. We let $\delta t = 1/N$. We compare the computed radial derivative to the exact value and observe errors shown in Table XIII. Since the sources are positioned at radius

TABLE XIII
Maximum Global Relative Errors for Sphere, $0 \le t \le 3$, for Second-, Fourth-, and Eighth-Order-Accurate Codes

N	$\delta\theta, \delta\phi$	2nd	4th	8th
42	$\pi/64$	$1.8 \times 10^{+0}$	$1.6 \times 10^{+0}$	$1.6 \times 10^{+0}$
63	$\pi/96$	6.5×10^{-1}	5.4×10^{-1}	5.4×10^{-1}
106	$\pi/160$	1.6×10^{-1}	5.6×10^{-2}	5.6×10^{-2}
170	$\pi/256$	6.1×10^{-2}	1.8×10^{-3}	1.6×10^{-3}
213	$\pi/320$	3.9×10^{-2}	4.1×10^{-4}	1.5×10^{-4}
266	$\pi/400$	2.5×10^{-2}	1.6×10^{-4}	1.3×10^{-5}

$r = \sqrt{0.5^2 + 0.8^2} \approx 0.94$, near the sphere $r = 1$ of interest, coarse spatial discretizations do not resolve the field. This effect is apparent in the fairly low accuracies, for small N, of all three temporal orders of discretization. As N increases, however, the spectral convergence of the spatial discretization yields very small spatial errors; the errors due to the second-, fourth-, and eighth-order-accurate temporal discretizations dominate.

6. CONCLUDING DISCUSSION

A new technique for efficiently applying the exact nonreflecting boundary conditions for the scalar wave equation was described and numerically tested in several boundary configurations. The technique is based on the observation that the nonreflecting boundary kernels for a planar, cylindrical, or spherical artificial boundary can be accurately approximated by compressed rational representations in the Laplace domain. A proof of the compression for the plane kernels was presented here; the cylinder and sphere kernels are treated elsewhere [3].

Our primary emphasis here was the demonstration of the performance of the boundary conditions in model wave-propagation problems, where comparisons to exact solutions and other boundary treatments were possible. In each case, for planar, circular, and spherical boundaries, in two and three dimensions, the accuracy obtained was consistent with essentially exact boundary conditions: the dominant source of error was spatial or temporal discretization error, and the error due to the boundary conditions was limited by the accuracy to which the boundary kernels were approximated.

The technique appears particularly advantageous when long time integrations are required, for the error that often accumulates with other boundary treatments is absent here. A particularly difficult example is the rectangle with periodic boundary conditions in one direction, for which a PML treatment is not very effective, but which is adequately handled by the new technique.

A primary limitation of the technique is that the propagation medium must be uniform at the boundary (any inhomogeneities must be confined). The technique does not suggest a way to treat propagation in infinite-layered media.

A secondary limitation is that the technique offers few choices for the shape of the artificial (nonreflecting) boundary. In particular, a general rectangular domain is not allowed. While this restriction need not ultimately limit which physical problems can be solved, it introduces some inconvenience in constructing modeling software, in addition to inefficiency for (otherwise) elongated domains. A melding of a Cartesian mesh with a circular or spherical boundary remains to be demonstrated.

The implementation of the boundary conditions for Maxwell's equations (following their formulation [20]), accurate discretization for scatterers with complicated shapes, the associated clustering of points (or small cells), and corresponding stability issues [4] remain problems for future research.

REFERENCES

1. J. D. Achenbach, Quantitative nondestructive evaluation, *Int. J. Solids Structures* **37**, 13 (2000).
2. B. Alpert, Hybrid Gauss-trapezoidal quadrature rules, *SIAM J. Sci. Comp.* **20**, 1551 (1999).
3. B. Alpert, L. Greengard, and T. Hagstrom, Rapid evaluation of nonreflecting boundary kernels for time-domain wave propagation, *SIAM J. Num. Anal.* **37**, 1138 (2000).

4. B. Alpert, L. Greengard, and T. Hagstrom, An integral evolution formula for the wave equation, *J. Comput. Phys.* **162**, 536 (2000).
5. A. Bayliss and E. Turkel, Radiation boundary conditions for wave-like equations, *Commun. Pure Appl. Math.* **23**, 707 (1980).
6. J. P. Berenger, Perfectly matched layer for the FDTD solution of wavestructure interaction problems, *IEEE Trans. Antennas Propagation* **44**, 110 (1996).
7. J.-P. Berenger, A perfectly matched layer for the absorption of electromagnetic waves, *J. Comput. Phys.* **114**, 185 (1994).
8. F. Collino and P. Monk, The perfectly matched layer in curvilinear coordinates, *SIAM J. Sci. Comput.* **19**, 2061 (1998).
9. M. D. Collins and W. A. Kuperman, Inverse problems in ocean acoustics, *Inverse Prob.* **10**, 1023 (1994).
10. B. Engquist and A. Majda, Absorbing boundary conditions for the numerical simulation of waves, *Math. Comput.* **31**, 629 (1977).
11. M. A. Epton and B. Dembart, Multipole translation theory for three-dimensional Laplace and Helmholtz equations, *SIAM J. Sci. Comput.* **16**, 865 (1995).
12. A. A. Ergin, B. Shanker, and E. Michielssen, Fast evaluation of three-dimensional transient wave fields using diagonal translation operators, *J. Comput. Phys.* **146**, 157 (1998).
13. O. P. Gandhi, G. Lazzi, and C. M. Furse, Electromagnetic absorption in the human head and neck for mobile telephones at 835 and 1900 MHz, *IEEE Trans. Microwave Theory Tech.* **44**, 1884 (1996).
14. D. Givoli, Nonreflecting boundary conditions, *J. Comput. Phys.* **94**, 1 (1991).
15. I. S. Gradshteyn and I. M. Ryzhik, *Tables of Integrals, Series, and Products* (Academic Press, New York, 1980).
16. L. Greengard, J. Huang, V. Rokhlin, and S. Wandzura, Accelerating fast multipole methods for low frequency scattering, *IEEE Comput. Sci. Eng.* **5**, 32 (1998).
17. R. O. Grondin, S. M. El-Ghazaly, and S. Goodnick, A review of global modeling of charge transport in semiconductors and full-wave electromagnetics, *IEEE Trans. Microwave Theory Tech.* **47**, 817 (1999).
18. M. Grote and J. Keller, Nonreflecting boundary conditions for time dependent scattering, *J. Comput. Phys.* **127**, 52 (1996).
19. J. J. Hack and R. Jakob, *Description of a Global Shallow Water Model Based on the Spectral Transform Method*, Technical Note TN-343 + STR (National Center for Atmospheric Research, Boulder, 1992).
20. T. Hagstrom, B. Alpert, L. Greengard, and S. I. Hariharan, Accurate boundary treatments for Maxwell's equations and their computational complexity, in *14th Annual Proceedings of Applied Computational Electromagnetics Society*, Monterey, CA, pp. 600–606 (1998).
21. T. Hagstrom, S. I. Hariharan, and R. C. MacCamy, On the accurate long-time solution of the wave equation in exterior domains: Asymptotic expansions and corrected boundary conditions, *Math. Comput.* **63**, 507 (1994).
22. T. Hagstrom, On high-order radiation boundary conditions, in *IMA Volume on Computational Wave Propagation*, edited by B. Engquist and G. Kriegsmann (Springer-Verlag, Berlin/New York, 1996), p. 1.
23. T. Hagstrom, Radiation boundary conditions for the numerical simulation of waves, *Acta Numer.* **8**, 47 (1999).
24. T. Hagstrom, Experiments with stable, high-order difference approximations to hyperbolic initial-boundary value problems, in *Proceedings of the Fifth International Conference on Mathematical and Numerical Aspects of Wave Propagation Phenomena*, edited by A. Bermudez, D. Gomez, C. Hazard, P. Joly, and J. Roberts (Soc. for Industr. & Appl. Math., Philadelphia, 2000).
25. B. Hu, W. C. Chew, E. Michielssen, and J. S. Zhao, Fast inhomogeneous plane wave algorithm for the fast analysis of two-dimensional scattering problems, *Radio Sci.* **34**, 759 (1999).
26. M. J. Mohlenkamp, A fast transform for spherical harmonics, *J. Fourier Anal. Appl.* **5**, 159 (1999).
27. M. Israeli and S. Orszag, Approximation of radiation boundary conditions, *J. Comput. Phys.* **41**, 115 (1981).
28. C. A. Langston, Wave-propagation theory and synthetic seismograms, *Rev. Geophys.* **29**, 662 (1991).
29. C. Lubich and A. Schädle, Fast convolution for non-reflecting boundary conditions, *SIAM J. Sci. Comput.* **24**, 161 (2002).

30. R. Mittra, W. D. Becker, and P. H. Harms, A general-purpose Maxwell solver for the extraction of equivalent-circuits of electronic package components for circuit simulation, *IEEE Trans. Circuits Systems I* **39**, 964 (1992).
31. J. J. Ottusch, G. C. Valley, and S. Wandzura, Integral equations and discretizations for waveguide apertures, *IEEE Trans. Antennas Propagation* **46**, 1727 (1998).
32. J. R. Phillips and J. K. White, A precorrected-FFT method for electrostatic analysis of complicated 3-D structures, *IEEE Trans. Comput. Aid. D* **16**, 1059 (1997).
33. P. Petropoulos, Reflectionless sponge layers as absorbing boundary conditions for the numerical solution of Maxwell's equations in rectangular, cylindrical and spherical coordinates, *SIAM J. Appl. Math.* **60**, 1037 (2000).
34. V. Rokhlin, Diagonal forms of translation operators for the Helmholtz equation in three dimensions, *Appl. Comput. Harmonic Anal.* **1**, 82 (1993).
35. V. S. Ryaben'kii, S. V. Tsynkov, and V. I. Turchaninov, *Global Discrete Artificial Boundary Conditions for Time-Dependent Wave Propagation*, Report 2001-14 (ICASE, 2001).
36. K. L. Shlager and J. B. Schneider, Selective survey of the finitedifference time-domain literature, *IEEE Trans. Antennas Propagation* **37**, 39 (1995).
37. I. L. Sofronov, Conditions for complete transparency on the sphere for the three-dimensional wave equation, *Russian Acad. Dci. Dokl. Math.* **46**, 397 (1993).
38. I. L. Sofronov, Artificial boundary conditions of absolute transparency for two- and three-dimensional external time-dependent scattering problems, *Eur. J. Appl. Math.* **9**, 561 (1998).
39. J. M. Song and W. C. Chew, Multilevel fast multipole algorithm for solving combined field integral equations of electromagnetic scattering, *Microwave Opt. Technol. Lett.* **10**, 14 (1994).
40. P. Stoica and R. L. Moses, *Introduction to Spectral Analysis* (Prentice–Hall, Englewood Cliffs, NJ, 1977).
41. L. Ting and M. Miksis, Exact boundary conditions for scattering problems, *J. Acoust. Soc. Am.* **80**, 1825 (1986).
42. K. Zhou, K. Glover, and J. C. Doyle, *Robust and Optimal Control* (Prentice–Hall, Englewood Cliffs, NJ, 1995).